A Fast and Efficient Method for Predicting Fluid Flow and Heat Transfer Problems

Peng Ding

Xue-Hong Wu

Ya-Ling He

Wen-Quan Tao
e-mail: wqtao@mail.xjtu.edu.cn

State Key Laboratory of Multiphase Flow and Heat Transfer,
School of Energy and Power Engineering,
Xi'an Jiaotong University,
Shaanxi 710049, P.R. China

A fast and efficient method based on the proper orthogonal decomposition (POD) technique for predicting fluid flow and heat transfer problems is proposed in this paper. POD is first applied to an ensemble of numerical simulation results at design parameters to obtain the empirical coefficients and eigenfunctions, and then the fluid and temperature fields in the range of design parameters are resolved by a linear combination of empirical coefficients and eigenfunctions. The empirical coefficients at off-design parameters are obtained by a cubic spline interpolation method for steady problems and a Galerkin projection method for transient problems. Finally, the efficiency and accuracy of the algorithm are examined by three examples. The POD based algorithm can predict both the velocity and temperature fields in the range of design parameters accurately at a price of a large number of precomputed cases (snapshots). It also brings significant computational time savings for the new cases within the parameter range presimulated compared with the finite volume method with SIMPLE-like algorithm.
[DOI: 10.1115/1.2804935]

Keywords: proper orthogonal decomposition, fast and efficient method, numerical simulation of fluid flow and heat transfer

1 Introduction

Many important applications in science and engineering need robust online control and performance optimization design; examples are the control of distribution of velocity and temperature fields in the tin bath of float process to increase glass quality, the control of mixing patterns in chemical vapor deposition (CVD) reactors to enhance the reactor performance, the viscous drag reduction to minimize the drag force, and the control of microelectrical mechanical structure (MEMS) to manipulate microflows and adjust the temperature distribution in the microsystems. Fluid flow and heat transfer are the predominant processes in these problems, which are governed by a series of partial differential equations with infinite degrees of freedom, e.g., Navier–Stokes equation for the flow field, energy equation for the temperature field, and convection-diffusion equations for other scalar variable fields; if turbulence is present, appropriate turbulence models must be employed. The system states, such as temperature, concentration, pressure, and velocity in these systems, are generally functions of space and time. These computational fluid dynamics (CFD)-type models have a direct physical interpretation and can estimate rather accurately the flow fields and temperature fields in a broad parameter range using numerical techniques, such as the finite volume method (FVM), by dividing the spatial and time domain into an enormous number of control volumes to achieve good accuracy. Generally, we use iterative solvers to obtain the solutions of resulting algebraic equations, but this requires a large amount of computation cost, and these models are too slow for following the dynamics of the actual physical process. Applying these CFD-type models into the industrial online predictive control and optimization design is still a challenging work.

A method that has received growing attention recently is the proper orthogonal decomposition (POD), which has been used for data analysis, data compression, and development of reduced order models of distributed parameter systems. The greatest attraction of the POD technique comes from its energy-optimality characteristic: i.e., among all possible decompositions of a physical field, with the same number of modes, POD modes will, on average, contain the most energy. Bleris and Kothare [1] studied the problem of regulation of thermal transient in a microsystem using empirical eigenfunctions obtained from the POD technique. In Ref. [2], Azeez and Vakakis used the POD technique to analyze the dynamic characteristic of two vibroimpacting systems. Kirby and Sirovich [3] employed the POD technique for the characterization of human faces. Allery et al. [4] used the POD technique to predict the indoor air quality. Arjocu and Liburdy [5] used the POD technique to identify major spatially distributed features of the heat transfer coefficient of a 3×3 square array of submerged, elliptic impinging jets. In Ref. [6], Tyagi and Acharya performed the large eddy simulations in a periodic domain of a rotating square duct with normal rib turbulators; then, the POD technique was applied to the resulting flow fields to investigate the low dimensionality of the system.

In this paper, we introduce the basic idea of POD first, and then we examine the feasibility and efficiency of the POD based algorithm for the prediction of fluid flow and heat transfer problems by three examples: (1) steady natural convection in a cavity with an aspect ratio of 2 in the Rayleigh number range of $5000-2\times10^5$, (2) steady lid-driven cavity problem with a Reynolds number range of 500–6000, and (3) transient nonlinear heat conduction problem with a time-dependent heat source. Finally, some conclusions will be drawn.

2 Fundamentals of the Proper Orthogonal Decomposition

The mathematical formulations of the POD presented in this section closely follow the one in Ref. [1]. The most crucial notion

Contributed by the Heat Transfer Division of ASME for publication in the JOURNAL OF HEAT TRANSFER. Manuscript received August 31, 2006; final manuscript received March 30, 2007; published online March 6, 2008. Review conducted by Louis C. Burmeister.

 Copyright © 2008 by ASME

Downloaded 26 Sep 2008 to 117.32.153.162. Redistribution subject to ASME license or copyright; see http://www.asme.org/terms/Terms_Use.cfm

of the POD is the snapshots $f(\mathbf{x},t_n)$, with $n=1,2,\ldots,N$ being a sample of solutions of the physical problem under consideration. The variable t represents some dependent variables; in transient problems it may denote the time variable, while in steady problems it may represent the Rayleigh number, Reynolds number, or such. It should be noted that the snapshots can be obtained either from the numerical simulation results or from experiments. Let us store a snapshot in a column vector with L entries. All snapshots of the system under consideration are stored in a rectangular $L \times N$ matrix $\{\mathbf{F}\}$.

The POD process aims at extracting a series of empirical eigenfunctions $\{\phi^k(\mathbf{x})_{k=1}^N\}$ and empirical coefficients $\alpha_k(t_k)$ from the snapshot matrix $\{\mathbf{F}\}$. According to the POD theory [7,8], the empirical eigenfunction $\phi(\mathbf{x})$ can be obtained by maximizing the normalized average projection of $\phi(\mathbf{x})$ onto $f(\mathbf{x},t_n)$. That is,

$$\text{Maximize}\left\{\lambda = \frac{\langle((\phi(\mathbf{x}),f(\mathbf{x},t_n))^2\rangle}{(\phi(\mathbf{x}),\phi(\mathbf{x}))}\right\} \tag{1}$$

where the brackets $\langle\cdot,\cdot\rangle$ mean the ensemble average of the snapshots and $(\cdot,\cdot)$ mean the standard Euclidean inner product. We define the linear operator H on $\phi(\mathbf{x})$ as

$$H\phi = \int_\Omega \frac{1}{N}\sum_{n=1}^{N} f(\mathbf{x},t_n)f(\mathbf{x}',t_n)\phi(\mathbf{x}')d\mathbf{x}' \tag{2}$$

then

$$(H\phi,\phi) = \int_\Omega\int_\Omega \frac{1}{N}\sum_{n=1}^{N} f(\mathbf{x},t_n)f(\mathbf{x}',t_n)\phi(\mathbf{x}')d\mathbf{x}'\phi(\mathbf{x})d\mathbf{x} \tag{3}$$

$$= \frac{1}{N}\sum_{n=1}^{N}\int_\Omega f(\mathbf{x},t_n)\phi(\mathbf{x})d\mathbf{x}\int_\Omega f(\mathbf{x}',t_n)\phi(\mathbf{x}')d\mathbf{x}' \tag{4}$$

$$= \frac{1}{N}\sum_{n=1}^{N}(f(\mathbf{x},t_n),\phi(\mathbf{x}))^2 \tag{5}$$

$$= \langle(\phi,f)^2\rangle \tag{6}$$

Thus, Eq. (1) can be written as

$$\text{Maximize}\left\{\lambda = \frac{\langle(H\phi,\phi)^2\rangle}{(\phi,\phi)}\right\} \tag{7}$$

Reference [7] shows that this leads to the eigenvalue problem of

$$\int_\Omega \frac{1}{N}\sum_{n=1}^{N} f(\mathbf{x},t_n)f(\mathbf{x}',t_n)\phi(\mathbf{x}')d\mathbf{x}' = \lambda\phi(\mathbf{x}') \tag{8}$$

Equation (8) can be solved by the direct method of Refs. [7,8]. While in practical numerical simulation, the resolution of the spatial domain is higher than the number of snapshots, directly evaluating the averaged autocorrelation function needs very large computation resources. A more accessible approach, which is referred to as the method of snapshots, was proposed by Sirovich [9]. This snapshot version of POD reduces the computation task to a much more tractable eigenvalue problem with a size of N equal to the number of the snapshots. The snapshot version of POD further makes the assumption that the spatial eigenfunctions are a linear combination of the snapshots

$$\phi^k(\mathbf{x}) = \sum_{n=1}^{N}\sigma_n^k f(\mathbf{x},t_n) \tag{9}$$

We introduce Eq. (9) into Eq. (8) which yields

$$\mathbf{A}\sigma^{(n)} = \lambda_n\sigma^{(n)} \quad n=1,\ldots,N \tag{10}$$

where $\mathbf{A}$ is an N-dimensional symmetric and positive semidefinite matrix. The elements of matrix $\mathbf{A}$ are defined as

$$A_{i,j} = \frac{1}{N}\int_\Omega f(\mathbf{x}',t_i)f(\mathbf{x}',t_j)d\mathbf{x}' \quad i=1,\ldots,N \quad j=1,\ldots,N \tag{11}$$

Now, the problem is reduced to finding the eigenvectors $\sigma^{(n)}$ of matrix $\mathbf{A}$, which can be easily solved by a standard numerical method. At last, Eq. (9) is used to resolve the empirical eigenfunction $\phi^k(\mathbf{x})$. According to the POD theory [7,8], the empirical eigenfunction $\phi^k(\mathbf{x})$ satisfies the following orthogonality condition:

$$(\phi^j(\mathbf{x}),\phi^j(\mathbf{x})) = \delta_{ij} = \begin{cases} 1 & i=j \\ 0 & i\neq j \end{cases} \tag{12}$$

and the magnitude of eigenvalue λ_k provides a measure of the amount of energy captured by the corresponding eigenfunction $\phi^k(\mathbf{x})$, while the energy measures the contribution of each eigenfunction to the overall system dynamics. So, in practice, we often order the eigenfunctions $\phi^k(\mathbf{x})$ by the magnitude of their corresponding eigenvalues λ_k, i.e., $\lambda_1>\lambda_2>\cdots>\lambda_N$.

Then, the snapshots of the system under consideration can be reconstructed by a combination of the eigenvectors as follows:

$$f(\mathbf{x},t_n) = \sum_{k=1}^{N}\alpha_k(t_n)\phi^k(\mathbf{x}) \tag{13}$$

where $\alpha_k(t_n)$ is the empirical coefficient, which can be analytically found by projecting flow fields (or any fields to be solved) onto each eigenfunctions,

$$\alpha_k(t_n) = (f(\mathbf{x},t_n),\phi^k(\mathbf{x})) \tag{14}$$

The reconstruction formula (Eq. (13)) may be truncated at a truncation degree of M as

$$f(\mathbf{x},t_n) = \sum_{k=1}^{M}\alpha_k(t_n)\phi^k(\mathbf{x}) \quad M\leqslant N \tag{15}$$

We define the participant energy coefficient ξ_n and the cumulative energy coefficient η_n as

$$\xi_n = \lambda_n \Big/ \sum_{n=1}^{N}\lambda_n \tag{16}$$

$$\eta_n = \sum_{n=1}^{M}\lambda_n \Big/ \sum_{n=1}^{N}\lambda_n \quad M\leqslant N \tag{17}$$

where ξ_n represents the energy in the total N modes that is contained in the nth eigenfunction, and η_n denotes the energy in the total N modes that is contained in the first n eigenfunctions. Generally, the truncation error will decrease with the increase of truncation degree M up to an optimal value; further increase in M will deteriorate the result since eigenfunctions with large index are contaminated by a roundoff error.

Now, we can summarize the POD based algorithm as follows.

1. Construct the snapshot matrix.
2. Solve the eigenvalue problem $\mathbf{A}\sigma^{(n)}=\lambda_n\sigma^{(n)}$, $n=1,\ldots,N$.
3. Resolve the eigenfunctions by $\phi^k(\mathbf{x})=\Sigma_{n=1}^N\sigma_n^k f(\mathbf{x},t_n)$.
4. Resolve the empirical coefficient $\alpha_k(t_n)$.
5. Reconstruct the physical fields by $f(\mathbf{x},t_n)=\Sigma_{k=1}^M\alpha_k(t_n)\phi^k(\mathbf{x})$.

3 Example 1: Natural Convection in a Cavity

In this section, we consider the problem of natural convection of fluid in a two-dimensional cavity. Natural convection is a challenging and complex problem due to the inherent coupling of the fluid flow and the energy transport. The geometry of the cavity and boundary conditions are schematically shown in Fig. 1. The height h of the cavity is two times of the width w of the short

Downloaded 26 Sep 2008 to 117.32.153.162. Redistribution subject to ASME license or copyright; see http://www.asme.org/terms/Terms_Use.cfm

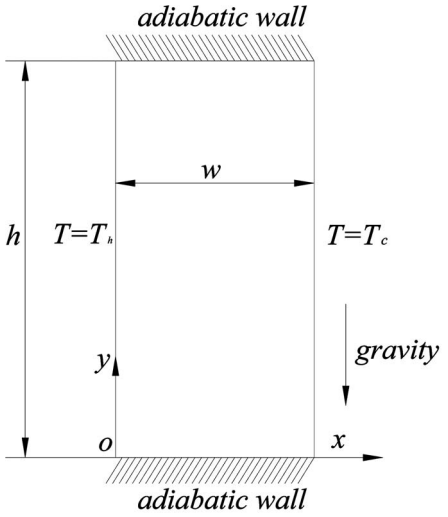

Fig. 1 Geometry of the cavity and boundary conditions, $h/w=2$

horizontal wall. The fluid in the cavity is air with a constant Pr number of 0.71. The left wall of the cavity is kept at a constant temperature T_h and the right wall at a constant lower temperature T_c. The other two surfaces are treated as adiabatic walls.

The equations governing the flow and temperature fields are those that express the conservation of mass, momentum, and energy. The flow, driven by buoyant forces, is assumed to be steady, laminar, and incompressible. The fluid properties are assumed constant, except for the density in the buoyancy term, where the Boussinesq approximation is valid. The mathematical formulation for this physical problem can be written in dimensionless form as

$$\frac{\partial U}{\partial X}+\frac{\partial V}{\partial Y}=0 \tag{18}$$

$$\frac{\partial (UU)}{\partial X}+\frac{\partial (UV)}{\partial Y}=-\frac{\partial P}{\partial X}+\frac{\partial^2 U}{\partial X^2}+\frac{\partial^2 U}{\partial Y^2} \tag{19}$$

$$\frac{\partial (UV)}{\partial X}+\frac{\partial (VV)}{\partial Y}=-\frac{\partial P}{\partial Y}+\frac{\partial^2 V}{\partial X^2}+\frac{\partial^2 V}{\partial Y^2}+\frac{\mathrm{Ra}}{\mathrm{Pr}}\theta \tag{20}$$

$$\frac{\partial (U\theta)}{\partial X}+\frac{\partial (V\theta)}{\partial Y}=\frac{1}{\mathrm{Pr}}\left(\frac{\partial^2 \theta}{\partial X^2}+\frac{\partial^2 \theta}{\partial Y^2}\right) \tag{21}$$

where the following dimensionless parameters are introduced:

$$X=\frac{x}{w} \quad Y=\frac{y}{w} \quad U=\frac{uw}{\nu} \quad V=\frac{vw}{\nu} \quad P=\frac{pw^2}{\rho\nu^2} \tag{22}$$

$$\theta=\frac{T-T_c}{T_h-T_c} \quad \mathrm{Pr}=\frac{\nu}{\alpha} \quad \mathrm{Ra}=\frac{g\beta(T_h-T_c)w^3}{\nu\alpha} \tag{23}$$

The parameters g, α, β, and ν are the acceleration due to gravity, the thermal diffusivity of the fluid, the coefficient of thermal expansion, and the fluid kinetic viscosity, respectively.

The boundary conditions are $U=V=0$ on all rigid walls, $\theta=1$ at $X=0$, $\theta=0$ at $X=1$, and $\partial\theta/\partial\mathbf{n}=0$ on the insulation walls, where $\mathbf{n}$ means the normal direction of walls.

The governing equations for mass, momentum, and energy are discretized by the widely used FVM [10,11]. The SIMPLE algorithm [10–12] is utilized for the treatment of the pressure-velocity coupling for the computation of the velocity and pressure fields on stagger grids. A high order QUICK [11,13] scheme is used to model the convective fluxes across the volume faces, and the conventional central difference scheme is used to approximate the diffusion terms. The set of linearized difference equations is solved with the tridiagonal matrix algorithm (TDMA). In this study, we use a 50×100 grid system, which is fine enough for the present problems, and the grid points are concentrated near the rigid walls where large physical variable gradients are expected. The computer code is validated by comparing the solutions with the benchmark solutions [14] for the case of natural convection in a square cavity, and the agreement is very good. For the simplicity of presentation, the results are not shown here since the main objective of this paper is the POD based algorithm.

3.1 Results and Discussion. The computations are first conducted at Rayleigh numbers from 5000 to 200,000 in increments of 5000, which gives a total of 40 solutions. In this example, the POD procedure is applied to the fluctuation part of the solutions. To do this, the average vector of the 40 solutions is first resolved as follows:

$$\bar{f}=\frac{1}{N}\sum_{n=1}^{N} f(\mathbf{x},t_n) \tag{24}$$

We form the snapshots by subtracting the average vector from the 40 solutions; then, the snapshots are assembled into the temperature snapshot matrix and the velocity snapshot matrix,

$$\Theta=\begin{bmatrix} \theta_{11} & \cdots & \theta_{1N} \\ \vdots & \ddots & \vdots \\ \theta_{L1} & \cdots & \theta_{LN} \end{bmatrix} \tag{25}$$

$$\mathbf{V}=\begin{bmatrix} U_{11} & \cdots & U_{1N} \\ V_{11} & \cdots & V_{1N} \\ \vdots & \ddots & \vdots \\ U_{L1} & \cdots & U_{LN} \\ V_{L1} & \cdots & V_{LN} \end{bmatrix} \quad N=1,\ldots,40 \tag{26}$$

As stated in Sec. 2, each column vector of the matrix represents the temperature or the velocity fields at a different design parameter, i.e., different Rayleigh number. Each row of the matrix represents the value of temperature at a specified grid point for different Ra numbers. There are a total of L rows for the temperature snapshot matrix and $2L$ rows in the velocity snapshot matrix since the velocity vector $\mathbf{V}$ has two components U and V, where U corresponds to the velocity in the x direction and V corresponds to the velocity in the y direction. The POD procedure is applied to these snapshot matrix to obtain the eigenfunctions $\phi_\theta(\mathbf{x})$ and $\phi_\mathbf{V}(\mathbf{x})$.

The velocity and the temperature fields can be expressed as a linear combination of the eigenfunctions $\phi_\theta(\mathbf{x})$, $\phi_\mathbf{V}(\mathbf{x})$ and the empirical coefficients as follows:

$$\theta^n_{\mathrm{POD}}(\mathbf{x})=\bar{\theta}+\sum_{k=1}^{M}\alpha_k(t_n)\phi^k_\theta(\mathbf{x}) \quad M\leqslant N \tag{27}$$

$$\mathbf{V}^n_{\mathrm{POD}}(\mathbf{x})=\bar{V}+\sum_{k=1}^{M}\beta_k(t_n)\phi^k_\mathbf{V}(\mathbf{x}) \quad M\leqslant N \tag{28}$$

To quantify the accuracy of the reconstruction formulas (Eqs. (27) and (28)), we define the relative error E as

$$E=\frac{\|f-f_{\mathrm{POD}}\|}{\|f\|} \tag{29}$$

where f means the finite volume solutions of the governing equations, and f_{POD} the solutions by means of the POD based algorithm; $\|\cdot\|$ means the L_2 norm.

In order to examine the accuracy of the POD at the off-design parameters, i.e., to test whether the POD procedure can be used to resolve the fluid and temperature fields at any Rayleigh numbers

Downloaded 26 Sep 2008 to 117.32.153.162. Redistribution subject to ASME license or copyright; see http://www.asme.org/terms/Terms_Use.cfm

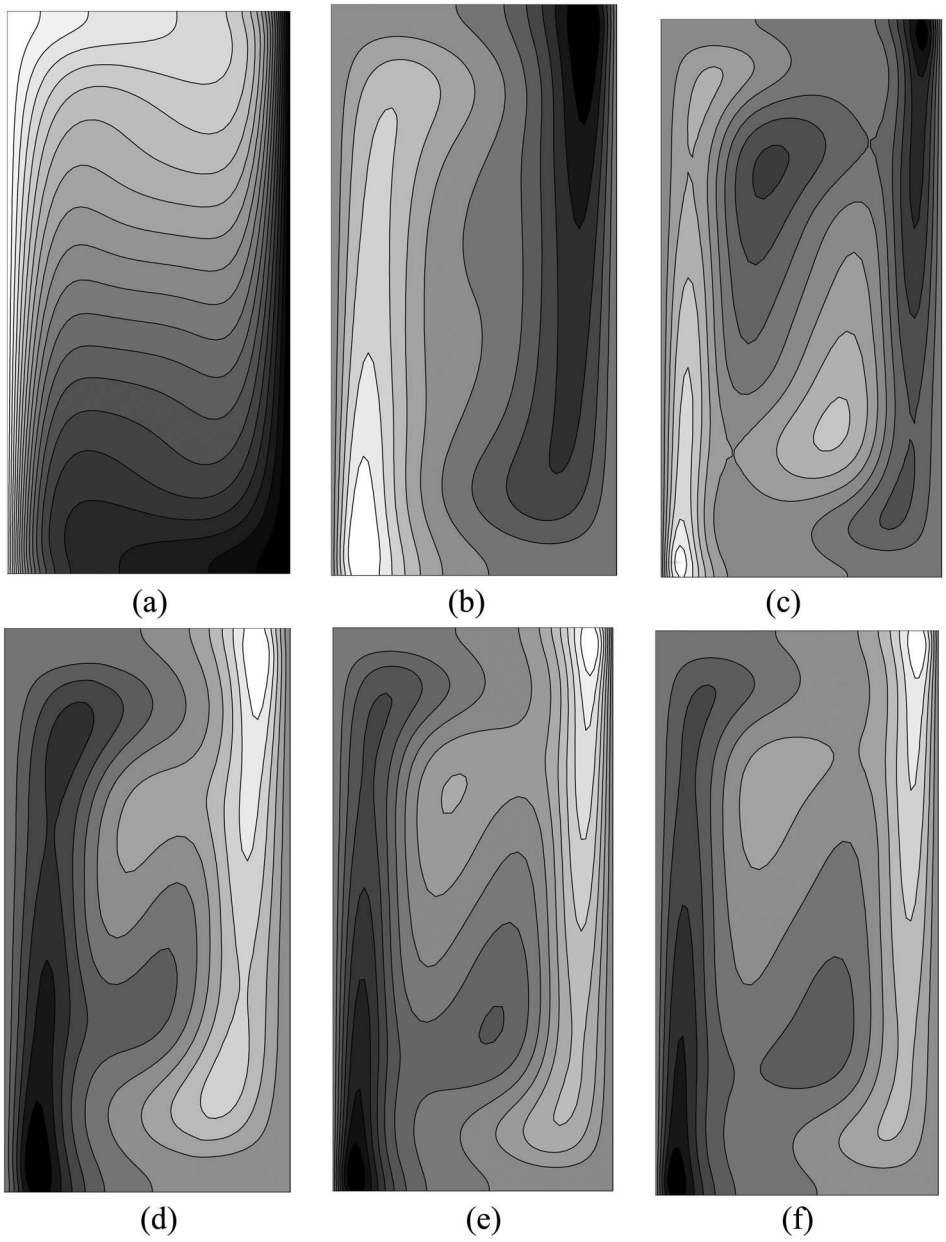

Fig. 2 Snapshots of temperature fields. (*a*) corresponds to the average temperature profile; (*b*)–(*f*) correspond to the fluctuation temperature fields at Ra=5000, Ra=50,000, Ra=100,000, 150,000, and Ra=200,000, respectively.

in the range of 5000 to 200,000, we also solve the governing equations at several representative Rayleigh numbers of 8150, 17,000, 85,700, and 168,800.

The average temperature field and the snapshots at Ra=5000, 50,000, 100,000, 150,000, and 200,000 are shown in Fig. 2. A total of 40 eigenvalues and 40 sets of eigenfunctions are obtained from the POD procedure. We arrange the eigenvalues according to their magnitude as $\lambda_1 \geqslant \lambda_2 \geqslant \cdots \geqslant \lambda_{40}$, and the first five largest eigenvalues of the temperature snapshots are listed in Table 1

Table 1 Eigenvalue and the energy distribution of velocity and temperature snapshots

n		1	2	3	4	5
ξ_n (%)	**U**	97.23	2.55	1.98×10^{-1}	1.29×10^{-2}	1.15×10^{-3}
	θ	95.44	4.28	2.09×10^{-1}	5.69×10^{-2}	3.06×10^{-3}
η_n (%)	**U**	97.233654	99.787496	99.985793	99.998766	99.999999
	θ	95.446871	99.730288	99.939785	99.996691	99.999756
λ_n	**U**	934,525.87	24545.32	1905.80	124.67	11.11
	θ	7.0941	0.3183	1.55×10^{-2}	4.22×10^{-3}	2.27×10^{-4}

Downloaded 26 Sep 2008 to 117.32.153.162. Redistribution subject to ASME license or copyright; see http://www.asme.org/terms/Terms_Use.cfm

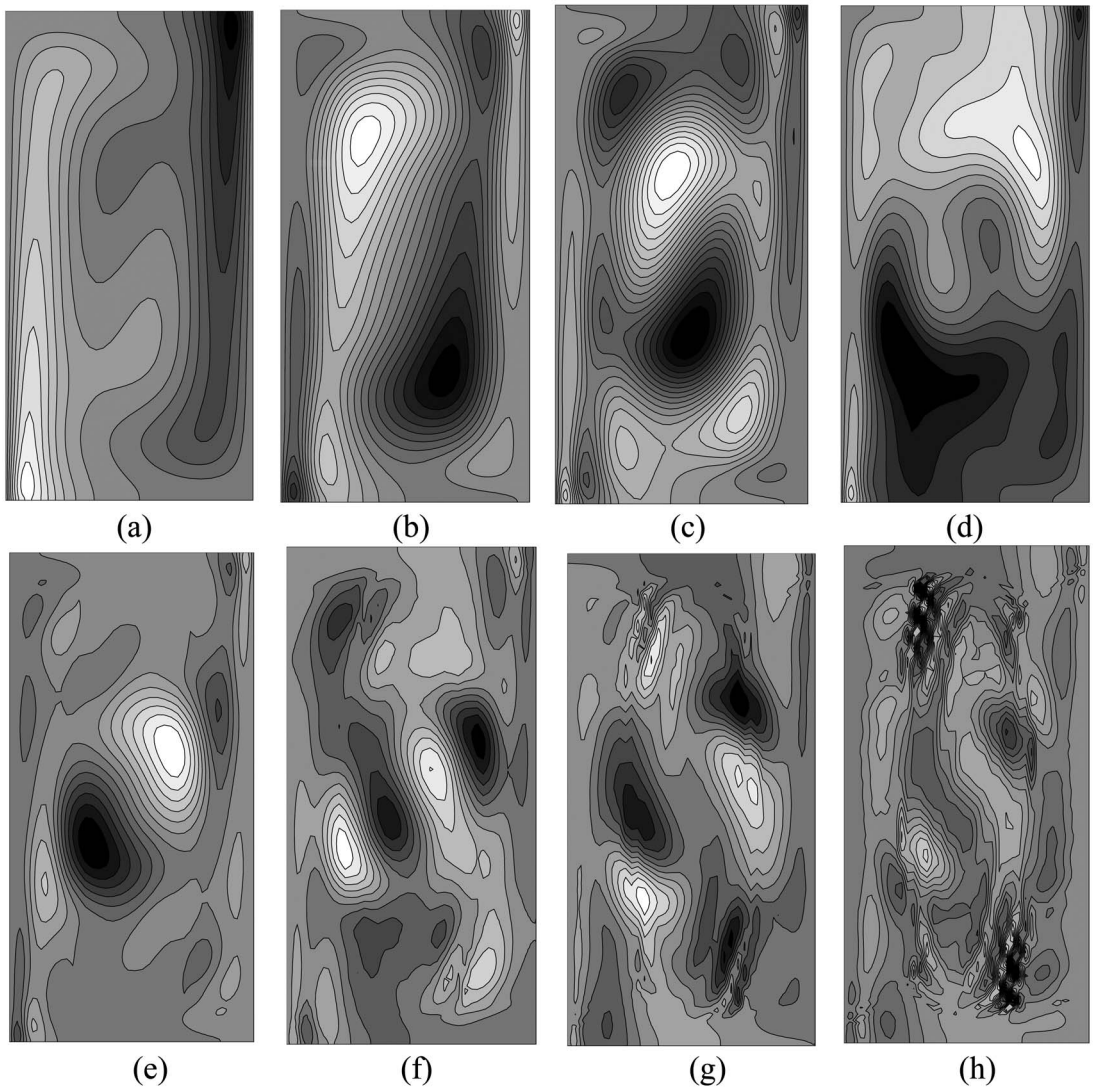

Fig. 3 The most dominant eight eigenfunctions obtained from the temperature snapshots by the POD technique

together with the participant energy coefficient ξ_n and the cumulative energy coefficient η_m. The energy optimality of the POD eigenfunctions is obvious in Table 1. For the temperature modes, it shows that the first eigenvalue have the largest magnitude and the most participant energy, and it alone captures 95.4468% of the total energy. The magnitude of the eigenvalue decreases drastically from the first value of 7.0941 to the second value of 0.3183 and the third value of 1.5571×10^{-2}. The second eigenfunction captures only 4.2834% of the total energy. The cumulative energy of the first two eigenvalues has reached 99.73028%. The later eigenvalues have much smaller eigenvalue and participant energy coefficients. For example, the 15th eigenvalue has a magnitude of 7.8198×10^{-10} and captures only 1.0521×10^{-8}% of the total energy. These smaller eigenvalues represent the contribution of the small scale structures to the total energy and cannot be truncated arbitrarily. Turning to the eigenvalues and the energy distribution of the velocity snapshots, a comparison with the eigenvalues; and the energy distribution of temperature snapshots shows that the magnitude of the velocity eigenvalues is much larger than temperature eigenvalues; the first velocity eigenfunction captures more energy than the first temperature eigenfunction. The variation trend is the same as that of the temperature snapshots.

The first eight temperature eigenfunctions and velocity eigenfunctions obtained by the POD procedure are shown in Figs. 3 and 4, respectively. Among all the eigenfunctions shown in Figs. 3 and 4, the eigenfunctions with large eigenvalues take the shape of large scale smooth structures, while the eigenfunctions with large index numbers have a tendency to include more small scale structures, and those small scale structures represent the structures not captured by the eigenfunctions of large eigenvalues, such as the velocity boundary layer or temperature boundary layer.

It should be noted that for the problems studied in this paper, there is no essential difference between applying the POD procedure to the fluctuation part and to the whole variable. Often, applying the POD procedure to the whole variable is more straightforward. We apply POD to the fluctuation part here just to show the versatility of the POD application.

3.2 Reconstruction and Extrapolation. The snapshots at the design parameters can be constructed by use of the reconstruction formula (Eqs. (27) and (28)). Since we have obtained the numerical solutions of velocity and the temperature fields at design conditions by FVM, we can resolve the empirical coefficients α_k and β_k analytically by projecting physical fields onto the POD eigenfunctions.

Figure 5 shows the logarithm of relative error E with 10 as the

Downloaded 26 Sep 2008 to 117.32.153.162. Redistribution subject to ASME license or copyright; see http://www.asme.org/terms/Terms_Use.cfm

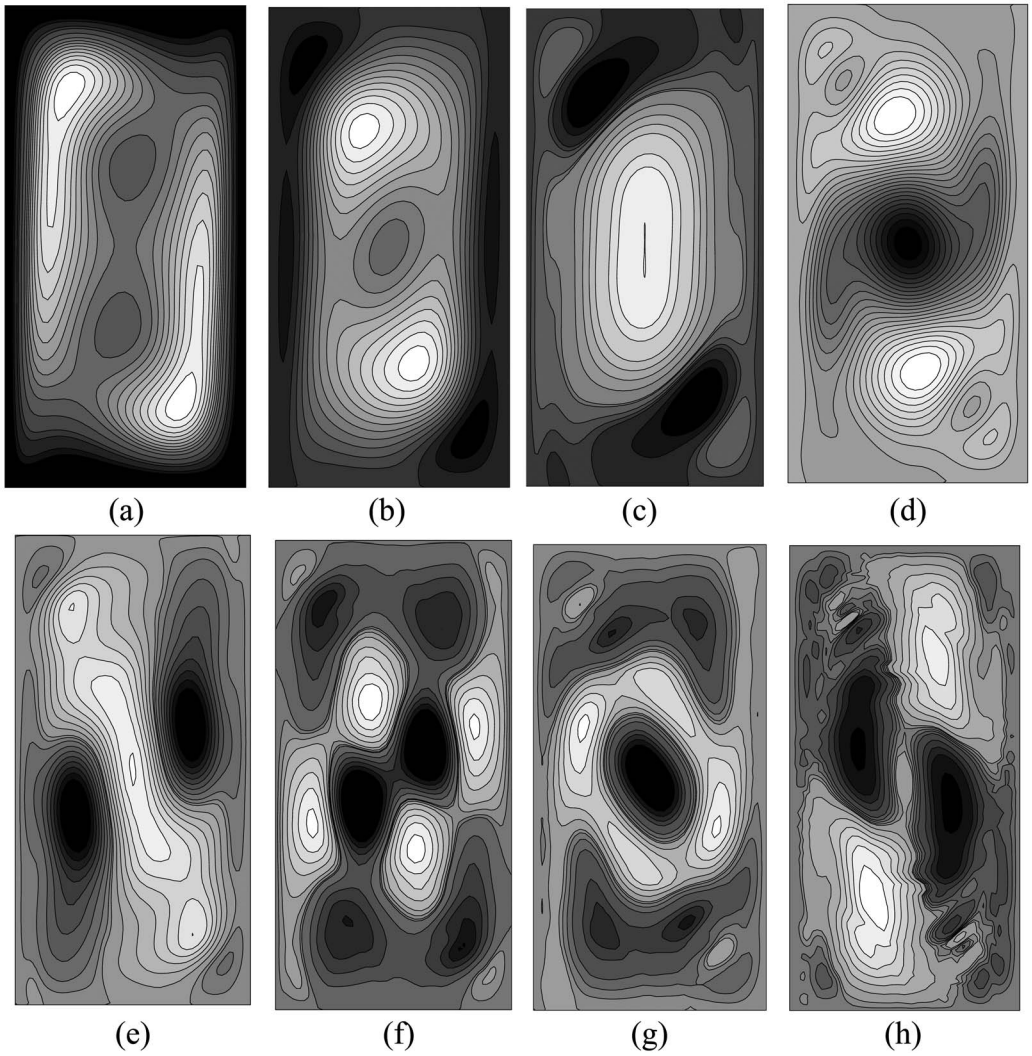

Fig. 4 The most dominant eight eigenfunctions obtained from the velocity snapshots by the POD technique (in streamline format)

base, between the numerical solutions obtained by FVM and the solutions obtained by POD procedure, where Fig. 5(*a*) corresponds to the relative error of temperature fields and Fig. 5(*b*) corresponds to the relative error of two components of the velocity fields. An overview of Fig. 5 shows that the physical fields can be reconstructed very well using the POD eigenfunctions as a basis. The relative error E decreases drastically as the increase of the truncation degree M, and the value of E takes the largest at the first few snapshots. For the temperature fields, with $M=4$, the relative error E is already less than 0.05%; the value of E may reach an order of 10^{-10} with $M=39$. There seems to be an increase in error when $M=40$ since the eigenfunctions with high index numbers may be contaminated by a roundoff error; the same phenomenon also exists for the velocity fields.

However, in practice, there are many cases in which the governing parameters are within the ranges prespecified. Not any parameter is exactly the same as any of the computed snapshots. We now demonstrate that by using the same POD eigenfunctions obtained at the design parameters, we are able to accurately reconstruct the physical fields at off-design parameters, too. It is this remarkable feature that makes POD very useful for the fast and accurate prediction of the fluid flow and heat transfer problems occurring in many industry processes. Assuming that no numerical solutions of the governing equations exist at the off-design parameters for the time being, we cannot resolve the empirical coefficients by projecting physical solutions onto the eigenfunctions. In this work, we use another method to evaluate the empirical coefficients needed for the reconstruction formula. We first fit a cubic spline through all the empirical coefficients at the design conditions, and then the empirical coefficients at the off-design parameters can be obtained by evaluating the cubic spline.

It is worth noting that even in the range of the design parameters, it is not a simple thing to directly interpolate the original snapshots for the solution desired. This is because the problems that we treat are strongly nonlinear, and it is difficult to know how to interpolate two neighboring snapshots even for a case positioned in space between the two snapshots.

The reconstruction physical fields at off-design parameters computed by the POD technique with a truncation degree of $M=6$ are compared with the FVM solutions in Fig. 6, and the plots show a remarkably good agreement.

It is interesting to compare the CPU time required for the POD based algorithm with that of the SIMPLE algorithm when simulating the natural convection heat transfer in a cavity. Table 2 says that the POD based algorithm is 100 times faster than the SIMPLE algorithm; it is also easy to find that the computation time for the POD technique is almost independent of the Rayleigh number and the truncation degree since the reconstruction of the physical field is a simple algebraic operation. It is expected that for more complicated situations, the saving in computational time may be much

Downloaded 26 Sep 2008 to 117.32.153.162. Redistribution subject to ASME license or copyright; see http://www.asme.org/terms/Terms_Use.cfm

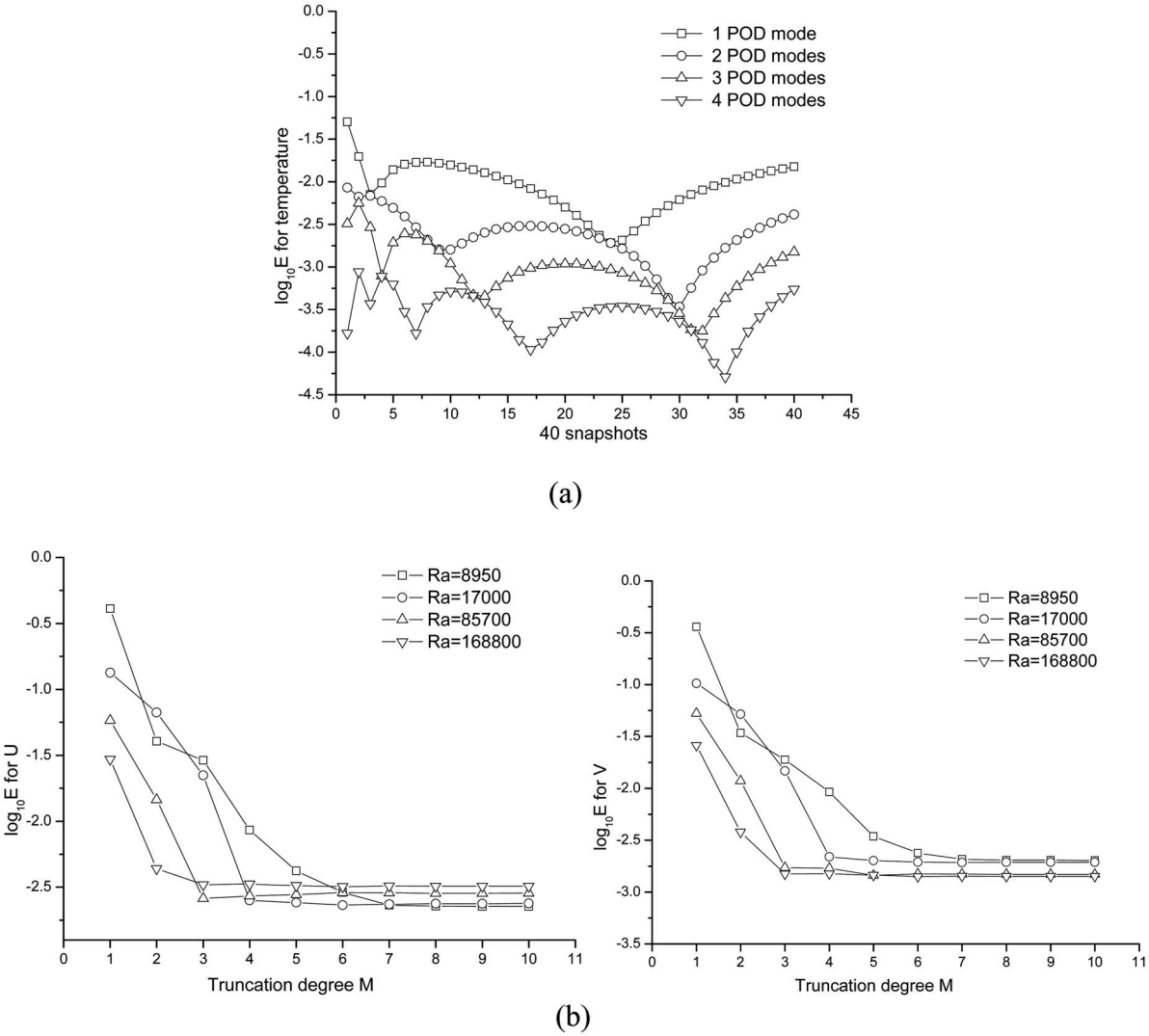

Fig. 5 The relative error between the numerical solutions and the POD reconstructions at design parameters. (*a*) corresponds to the relative error between the numerical temperature fields and the POD reconstruction fields of the 40 snapshots; (*b*) corresponds to relative error between the numerical velocity fields and the POD reconstruction fields of the 40 snapshots.

larger.

It should be noted that the computational time of each method was just picked up from the record in the computer. No conversion method was adopted between the FVM solution and the POD algorithm. This is because when both the POD and the FVM are used to provide information for the production control, it is this CPU computational time that makes sense. Of course, the process of creation of snapshots for POD based algorithm may consume a lot of computational resource and time. This is the expense that we pay for the later fast usage, and it is like the learning process or training process. However, once enough snapshots are collected, we may adopt the POD technique to obtain the required information in a very short time period. It is this quick response that is highly desired for control of a practical production process. By directly adopting the transient and multidimensional simulations in situ, we could not acquire the desired information in time although a lot of computational resource and time should also be paid. In addition, after the training process, a series of robust eigenfunctions and empirical coefficients can be used many times, and are valid over a useful range of governing parameters.

4 Example 2: Lid-Driven Cavity Flow

In this section, we consider a lid-driven cavity flow problem [15]. Figure 7 shows a schematic view of the cavity flow and its boundary conditions. The governing equations can be written in a dimensionless form as follows:

$$\frac{\partial U}{\partial X}+\frac{\partial V}{\partial Y}=0 \tag{30}$$

$$\frac{\partial (UU)}{\partial X}+\frac{\partial (UV)}{\partial Y}=-\frac{\partial P}{\partial X}+\frac{1}{\mathrm{Re}}\left(\frac{\partial^2 U}{\partial X^2}+\frac{\partial^2 U}{\partial Y^2}\right) \tag{31}$$

$$\frac{\partial (UV)}{\partial X}+\frac{\partial (VV)}{\partial Y}=-\frac{\partial P}{\partial Y}+\frac{1}{\mathrm{Re}}\left(\frac{\partial^2 V}{\partial X^2}+\frac{\partial^2 V}{\partial Y^2}\right) \tag{32}$$

where the characteristic length and characteristic velocity are the width of the cavity and the velocity of the lid, respectively.

The boundary conditions are

$$U=1, V=0 \quad \text{on the lid} \tag{33}$$

Downloaded 26 Sep 2008 to 117.32.153.162. Redistribution subject to ASME license or copyright; see http://www.asme.org/terms/Terms_Use.cfm

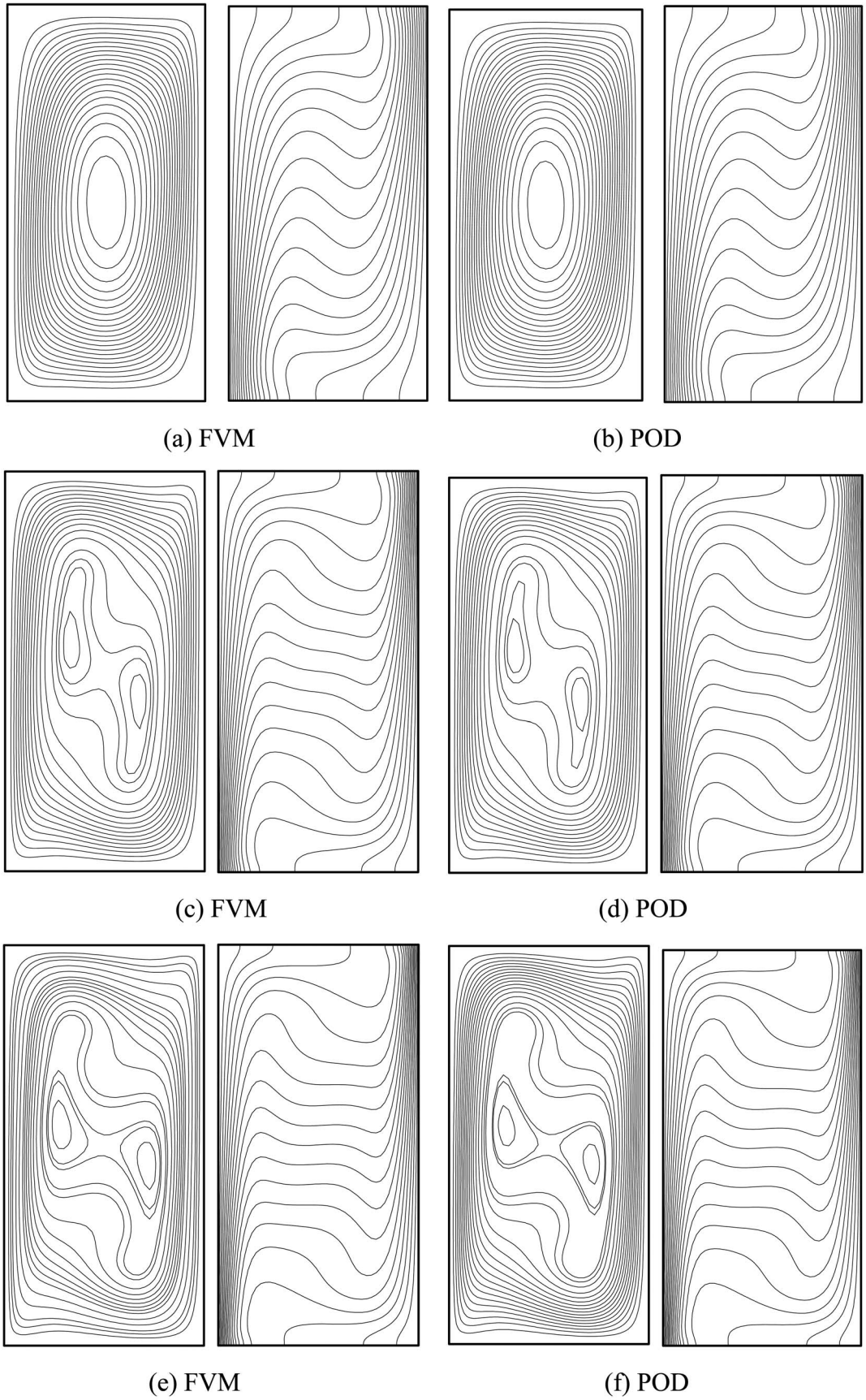

Fig. 6 Comparison between the POD and the FVM solutions for Ra numbers at off-design parameters, with *M*=6. (*a*) and (*b*) correspond to the streamline and isothermal at Ra=17,000; (*c*) and (*d*) correspond to the streamline and isothermal at Ra=85,700; (*e*) and (*f*) correspond to streamline and isothermal at Ra=168,800.

Downloaded 26 Sep 2008 to 117.32.153.162. Redistribution subject to ASME license or copyright; see http://www.asme.org/terms/Terms_Use.cfm

Table 2 Comparison of computation time between SIMPLE and POD (seconds)

Rayleigh number	8950	17,000	85,700	168,800
SIMPLE	137.36	131.08	117.96	116.09
POD with one mode	1.42	1.38	1.50	1.53
POD with five modes	1.45	1.49	1.53	1.49
POD with ten modes	1.53	1.56	1.56	1.56

$$U = 0, V = 0 \quad \text{on the wall} \tag{34}$$

It may be noted that although the lid-driven cavity flow is a pure fluid problem, it is still worth adopting this problem as an example. This is because the lid-driven cavity flow is a kind of classical problem in CFD and heat transfer area, and its benchmark solutions exist [15]. In addition, in many heat transfer problems, the working medium can be treated as one with constant thermophysical properties, and for such problems the solution of velocity fields is of crucial importance to obtain the temperature field. Therefore, we take this example to further verify the feasibility of POD for fluid flow and heat transfer problems.

4.1 Results and Discussion. The discretized equations are solved on an 80×80 grid system with the same numerical method and discretization scheme as that of Example 1. The solutions are obtained at Reynolds number from 500 to 6000 in increments of 500, which gives a total of 12 snapshots. Then, the POD technique is applied to these 12 snapshots to obtain the eigenvalues and eigenfunctions. In addition, numerical solutions at three off-design parameters corresponding to Re=800, 2700, and 5300 are also obtained.

Table 3 gives the first five largest eigenvalues, together with the participant energy coefficient ξ_n and the cumulative energy coefficient η_n. An overview of Table 3 shows that the same trend exists for the natural convection problem in Example 1. A comparison between Tables 1 and Table 3 shows that there is a big difference between the magnitudes of corresponding eigenvalues, the participant energy coefficient ξ_n and the cumulative energy coefficient η_n.

Figure 8 shows the first six dominant velocity eigenfunctions obtained from the POD technique. It is obvious that the eigenfunctions with large eigenvalues represent large scale flow structures, while the later eigenfunctions contain more and more small vortexes.

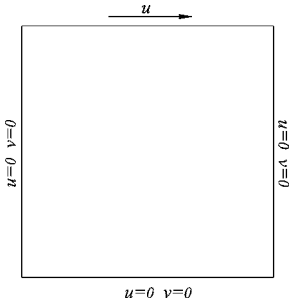

Fig. 7 Schematic view of driven cavity flow

4.2 Reconstruction and Extrapolation. Figure 9 shows the logarithm of relative error E with 10 as the base, between the numerical solutions obtained by FVM and the solutions obtained by the POD technique. Again, the physical fields at the design parameters are reconstructed very well. The relative error decreases drastically as the truncation degree M increases. With the truncation degree $M=4$, the relative error E has reached a value of no more than 1%. When the truncation degree is 12, the relative error E if of the order of 10^{-10}.

The extrapolation performance of the POD is shown in Fig. 10. The empirical coefficients needed in the reconstruction formulations are resolved by the same procedure as that in Example 1. From an overview of Fig. 10, it can be seen that the reconstruction is also good. The relative error E takes the minimum value of no more than 0.3% at the optimal truncation degree of $M=6$. Figure 11 shows the streamline obtained by the FVM and the POD based algorithm at Re=5300. The plots show a remarkably good agreement.

In terms of computational time, it requires almost 37 s to obtain a solution by the FVM method, but only 0.45 s to obtain a solution by the POD based algorithm.

5 Example 3: Heat Conduction Problem With a Time-Dependent Heat Source

In this section, we consider a transient nonlinear heat conduction problem where the heat source is a function of time and the thermal conductivity is a function of temperature, making the problem nonlinear both in space and in time. It will be shown that we can predict the temperature fields accurately at every time instant when the heat source varies arbitrarily by utilizing the POD based algorithm. The nondimensional governing equation and boundary conditions are as follows:

$$\frac{\partial \theta}{\partial t} = \frac{\partial}{\partial x}\left(\kappa(\theta)\frac{\partial \theta}{\partial x}\right) + S(t,x) \tag{35}$$

The term $S(t,x)$ in Eq. (35) represents a time-dependent heat source, which is defined as

$$S(t,x) = f(t)n/2\cosh^2(n(x-x_o)) \tag{36}$$

The term $S(t,x)$ will become a point source located at $x=x_0$ as n reaches infinity. In this work, we take $n=100$ and $x_0=0.25$. The relevant initial and boundary conditions are

$$\theta(x,0) = 0.01 \tag{37}$$

$$\theta(0,t) = 0.0 \tag{38}$$

$$\theta(1,t) = 0.0 \tag{39}$$

The temperature dependent thermal diffusivity is given by

$$\kappa(\theta) = 1 + \sigma\theta \tag{40}$$

where σ is a constant at a value of 0.01. The function $f(t)$ represents the time-dependent part of the heat source term. In this paper, the value of the $f(t)$ varies in the range of 0–20.

5.1 Construction of Snapshots and Galerkin Projection. The governing equation is discretized by the FVM with 100 control volumes, and the unsteady term is discretized by the first-

Table 3 Eigenvalue and the energy distribution of velocity snapshots

n	1	2	3	4	5
ξ_n (%)	97.28	2.41	2.82×10^{-1}	2.74×10^{-2}	2.34×10^{-3}
η_n (%)	97.282010	99.687427	99.969250	99.996646	99.998995
λ_n	461.11	11.40	1.34	1.29×10^{-1}	1.11×10^{-2}

Downloaded 26 Sep 2008 to 117.32.153.162. Redistribution subject to ASME license or copyright; see http://www.asme.org/terms/Terms_Use.cfm

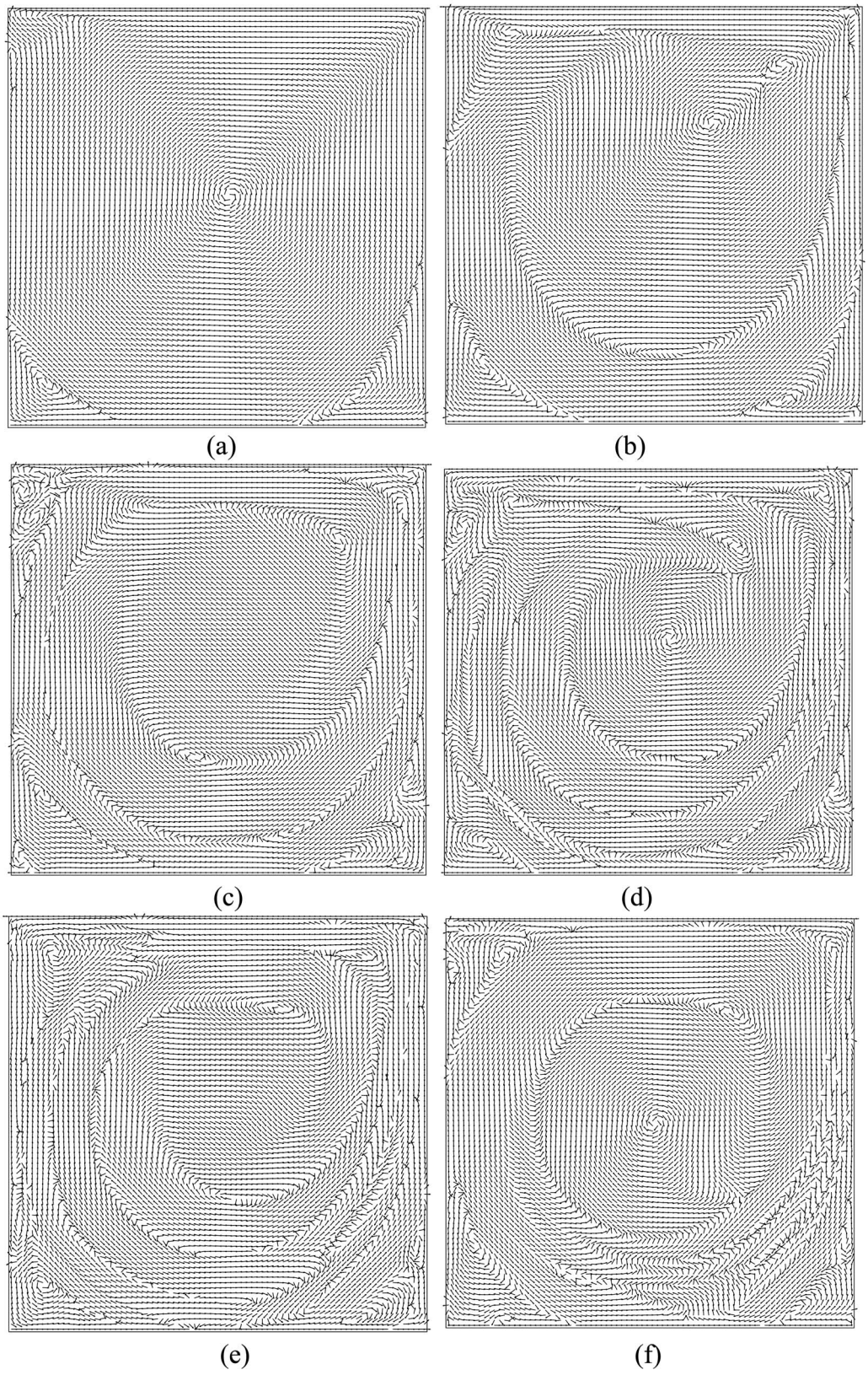

Fig. 8 The first six dominant velocity eigenfunctions obtained from the velocity snapshots by the POD technique

Downloaded 26 Sep 2008 to 117.32.153.162. Redistribution subject to ASME license or copyright; see http://www.asme.org/terms/Terms_Use.cfm

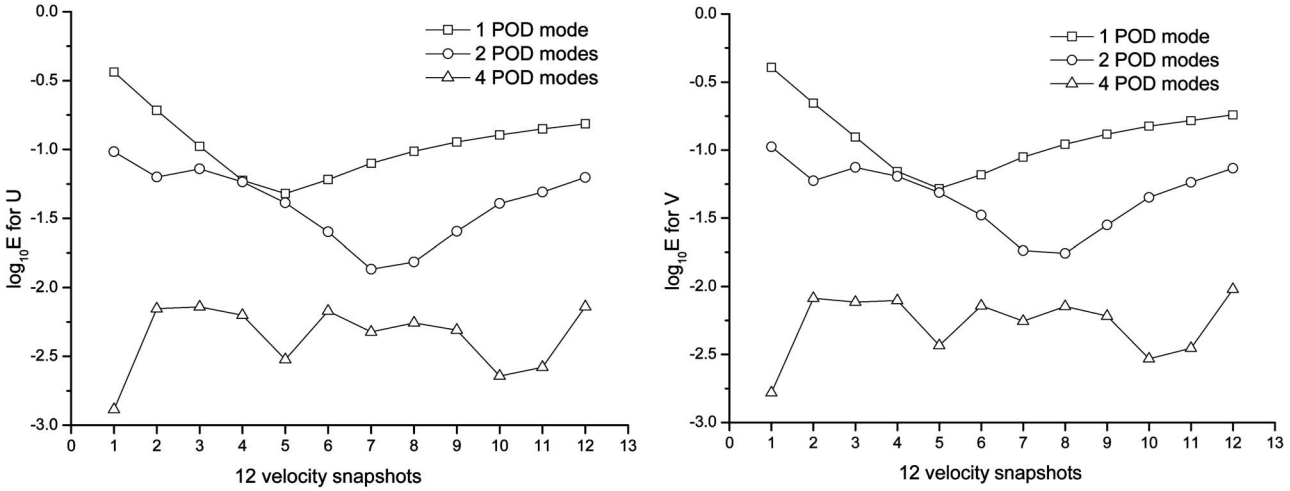

Fig. 9 The relative error between the numerical solution and the POD reconstruction at design parameters

order backward difference scheme. The set of discretized algebraic equations is solved by the Gaussian elimination method. Steady state is reached after 1520 time steps with a time step of $\Delta t = 0.0005$.

The construction of the snapshots is the most important step of the POD procedure for an unsteady problem since the eigenfunctions are obtained from the decomposition of the snapshot matrix. The snapshots must be representative of the dynamic characteristic of the system under consideration. We may take solutions at every time step as a snapshot, but it becomes impossible when we are solving very complex problems, e.g., the DNS of turbulence. In this problem, the temperature field varies greatly at the initial stage, and it varies less as time goes on. Thus, it is necessary to take more snapshots at the initial stage, and the number of the snapshots may be decreased as time elapses.

It will be demonstrated that the POD based algorithm can predict the temperature fields at off-design parameters very well with only 120 snapshots. We use the following method to take snapshots, 50 snapshots are obtained at the time interval of 0.0005 during the time period 0.000–0.025 s, other 50 snapshots are obtained at the time interval of 0.0055 during the time period 0.025–0.3 s, and the other 20 snapshots are obtained in the time period 0.3–0.76 s.

In Examples 1 and 2, we use a cubic spline polynomial to evaluate the empirical coefficients in the reconstruction formula. However, for the transient problem, the interpolation method cannot succeed. In order to get the empirical coefficients at the off-design parameters, a Galerkin procedure employing this empirical eigenfunction basis is applied to the governing equations. The Galerkin projection method can also be applied to the Navier–Stokes equations in Examples 1 and 2, but the method of cubic spline interpolation is very easy to implement and can give very accurate results.

First, we represent the temperature field θ as follows:

$$\theta(x,t) = \sum_{k=1}^{M} \alpha_k(t_n)\phi_\theta^k(x) \quad M \leqslant N \tag{41}$$

After substituting Eq. (41) into Eq. (35), applying the Galerkin procedure, and using the orthogonality property of eigenfunctions, we obtain

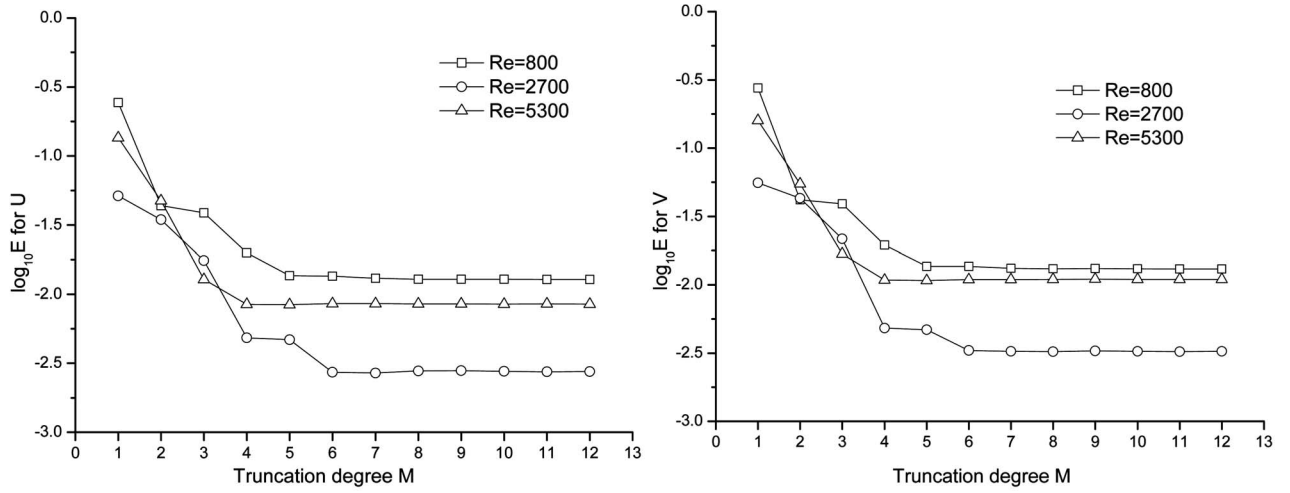

Fig. 10 Relative error versus the truncation degree *M* at off-design parameters

Downloaded 26 Sep 2008 to 117.32.153.162. Redistribution subject to ASME license or copyright; see http://www.asme.org/terms/Terms_Use.cfm

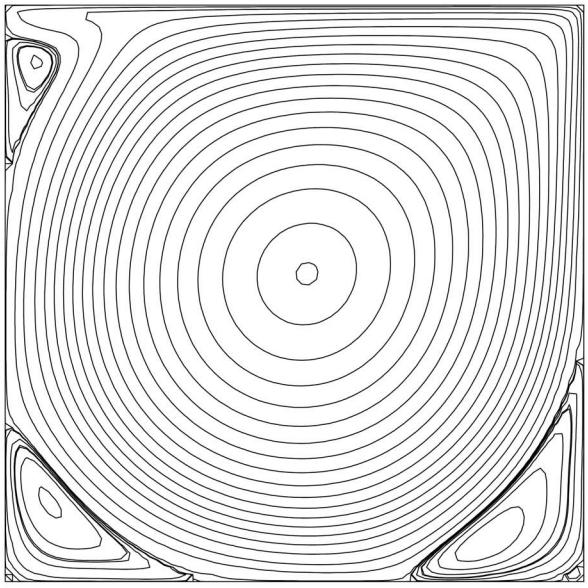

(a) FVM solution

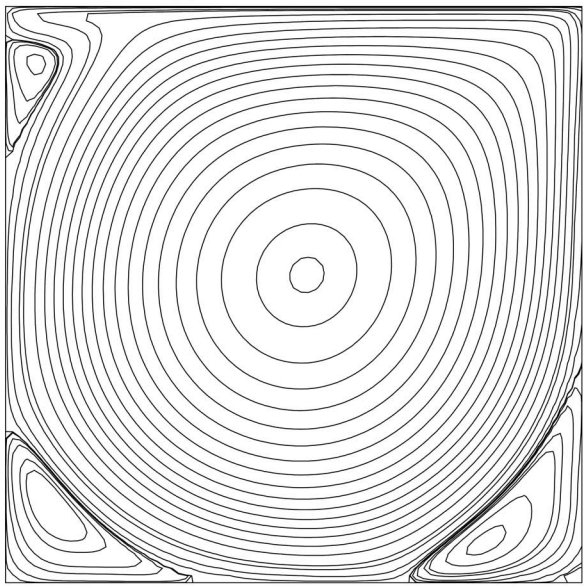

(b) POD solution

Fig. 11 Comparison between the POD and the FVM solutions for Re=5300 with *M*=6

$$\frac{d\alpha_i}{dt} = -\sum_{k=1}^{M} H_{ik}\alpha_k - \lambda \sum_{k=1}^{M}\sum_{l=1}^{M} Q_{ikl}\alpha_k\alpha_l + F_i \quad i = 1,2,\ldots,M \tag{42}$$

where

$$H_{ik} = \left(\frac{\partial \phi_i}{\partial x}, \frac{\partial \phi_k}{\partial x}\right) \tag{43}$$

$$Q_{ikl} = \left(\frac{\partial \phi_i}{\partial x}, \frac{\partial \phi_k}{\partial x}\right)\phi_l \tag{44}$$

$$F_i = (\phi_i, S(t,x)) \tag{45}$$

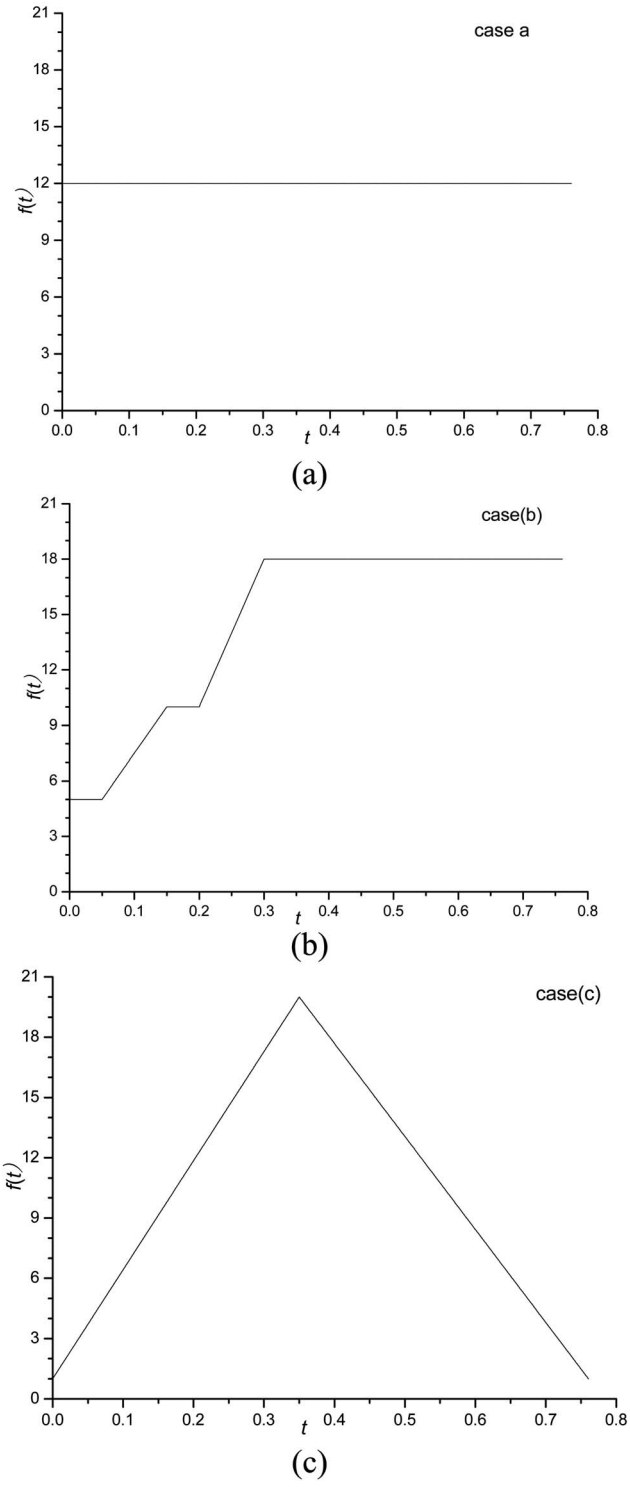

Fig. 12 Various shape of function *f*(*t*) used to examine the performance of the POD based algorithm. (*a*), (*b*), and (*c*) correspond to case (a), case (b), and case (c), respectively.

The ordinary differential (Eq. (42)) is solved by a sixth-order Runge–Kutta method with a time step of $\Delta t = 0.0005$. The initial value for the system is obtained by the projection of the initial value of θ onto the eigenfunctions,

$$\alpha_i(t_0) = (\theta(x,0), \phi_i) \tag{46}$$

Downloaded 26 Sep 2008 to 117.32.153.162. Redistribution subject to ASME license or copyright; see http://www.asme.org/terms/Terms_Use.cfm

Table 4 Eigenvalues and the energy distribution of temperature snapshots

n	1	2	3	4	5
ξ_n (%)	96.65	3.26	8.99×10^{-2}	4.42×10^{-3}	4.78×10^{-4}
η_n (%)	96.64582	99.90516	99.99507	99.99949	99.99997
λ_n	110.36	3.72	0.10	5.05×10^{-3}	5.46×10^{-4}

5.2 Results and Discussion. The POD procedure is applied to these 120 snapshots to yield eigenfunctions. Table 4 shows the first five dominant eigenvalues together with their participant energy coefficient ξ_n and the cumulative energy coefficient η_n at the design parameter $f(t)=20$. A comparison with the results of Examples 1 and 2 shows that the same trend exists for the transient problem; the first eigenvalue takes the largest value, and the corresponding eigenfunction captures the most energy. With the first five eigenfunctions, the cumulative energy coefficient η_n reaches a value of 99.99997%. Figure 13(*a*) gives the variation of the empirical coefficients $\alpha_i(t)$ with time for the case of $f(t)=20$. The empirical coefficients $\alpha_i(t)$ are obtained analytically by means of projection of the solutions onto the eigenfunctions. It is obvious that the first empirical coefficients $\alpha_1(t)$ vary in the smoothest way and the coefficients with large indices have large fluctuations during the initial stage, while both of them approach a constant value as the system reaches a steady state. The fourth empirical coefficient $\alpha_4(t)$ varies little with time and has a value very close to zero, which means that it contributes little to the reconstruction of the temperature fields. This can also be found in Table 4 since the fourth participant energy coefficient ξ_n has a value of 4.42×10^{-5}.

To examine the performance of the POD based algorithm, we consider three different cases of the time-dependent function $f(t)$, as shown in Fig. 12. In all these three cases, the empirical coefficients $\alpha_i(t)$ are obtained by solving Eq. (42) with an optimal truncation degree $M=6$; further increase in the value of the truncation degree M does not improve the accuracy of the reconstruction.

Figures 13(*b*)–13(*d*) give the shape of the empirical coefficients corresponding to case (a), case (b), and case (c), respectively. For case (a) and case (b), the variation of the empirical coefficients $\alpha_i(t)$ has the same pattern with that of the case at the design parameter. For case (d), the shape of the empirical coefficients takes a very different pattern since the time-dependent function $f(t)$ varies during the whole time interval of 0–0.76 s, and the system does not have a steady state.

Figures 14(*a*)–14(*c*) show the temporal variation of the relative error E for case (a), case (b), and case (c), respectively. From an overview of Fig. 14, it reveals that the relative error E takes the largest value at the initial stage, and there is also a large decrease of the error at the initial stage. As time elapses, the relative error E reduces to a constant value of no more than 0.8%. The variation of temperature at two points—$x=0.25$, which is close to the location of heat source, and $x=0.90$, which is close to the boundary for case (b) and case (c)—are indicated in Figs. 15(*a*) and 15(*b*). The agreement between the FVM solutions of the governing equation and the POD solutions is excellent.

In terms of computational time, about 8.63 s is required to obtain a solution by the FVM method and only 0.32 s is required to obtain a solution by the POD based algorithm. Further time saving can be expected when this method is applied to two-dimensional or three-dimensional nonlinear heat conduction problems.

6 Concluding Remarks

In this paper, an algorithm based on the POD, which can reduce the computation time tremendously for the prediction of the fluid flow and heat transfer problems without deteriorating accuracy, is developed. The performance of the algorithm is illustrated by three examples.

The empirical coefficients needed to reconstruct the physical fields can be obtained by an interpolation method for steady problems or the Galerkin projection method for transient problems.

It is observed that the relative error between the reconstruction physical fields and the exact physical fields can reach an order of 10^{-10} at the design parameters. For the physical fields at off-design parameters, the relative error can reach an order of 10^{-3} at least; for the scalar physical field the relative error may reach an order of 10^{-4}. It is this remarkable feature that makes the POD useful to control procedures where fluid flow and heat transfer dominate.

The optimal truncation degree is around $M=6$ in this investigation; further increase of the truncation degree does not affect the accuracy of the reconstruction.

The use of the POD based algorithm to predict the fluid and temperature fields yields a drastic time reduction compared with the FVM with SIMPLE algorithm. It is almost 100 times faster than the FVM, and it can be expected that the more complicated the process, the greater the saving in computational time.

Acknowledgment

This work was supported by the National Natural Science Foundation of China (Grant Nos. 50476046 and 50636050).

Nomenclature

h = height of the cavity
w = width of the cavity
H = linear operator defined in Eq. (4)
N = number of snapshots
M = truncation degree
Pr = Prandtl number
Ra = Rayleigh number
U = nondimensional velocity component in the x direction
V = nondimensional velocity component in the y direction
t = dependent variables
$\mathbf{n}$ = normal direction
$\mathbf{x}$ = vectors of coordinates
$\langle\cdot,\cdot\rangle$ = ensemble average
$(\cdot,\cdot)$ = inner product of two functions

Greek Symbols

ξ = participant energy coefficient
η = cumulative energy coefficient
λ = eigenvalues
θ = nondimensional temperature
ϕ = eigenfunction

Downloaded 26 Sep 2008 to 117.32.153.162. Redistribution subject to ASME license or copyright; see http://www.asme.org/terms/Terms_Use.cfm

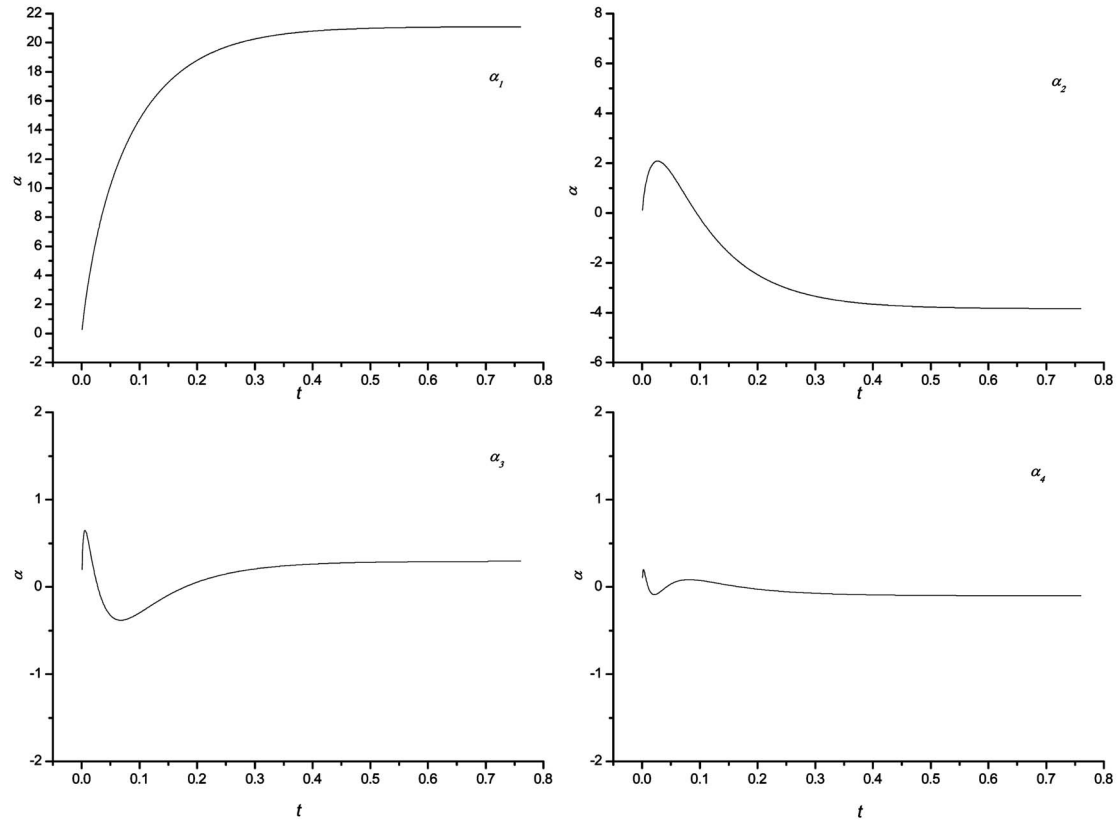

(a)

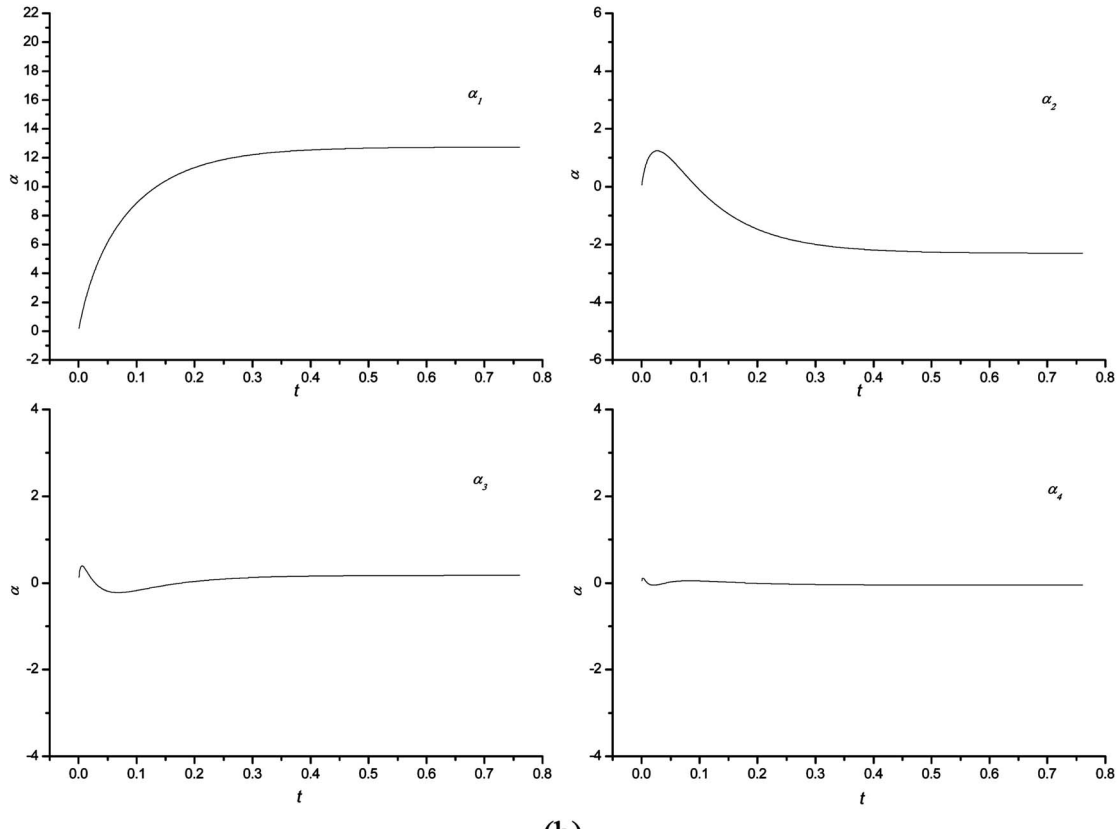

(b)

Fig. 13 The variation of empirical coefficients as a function of time. (*a*) corresponds to the function $f(t)=20$ at design parameters; (*b*), (*c*), and (*d*) correspond to function $f(t)$ at case (a), case (b), and case (c), respectively.

Downloaded 26 Sep 2008 to 117.32.153.162. Redistribution subject to ASME license or copyright; see http://www.asme.org/terms/Terms_Use.cfm

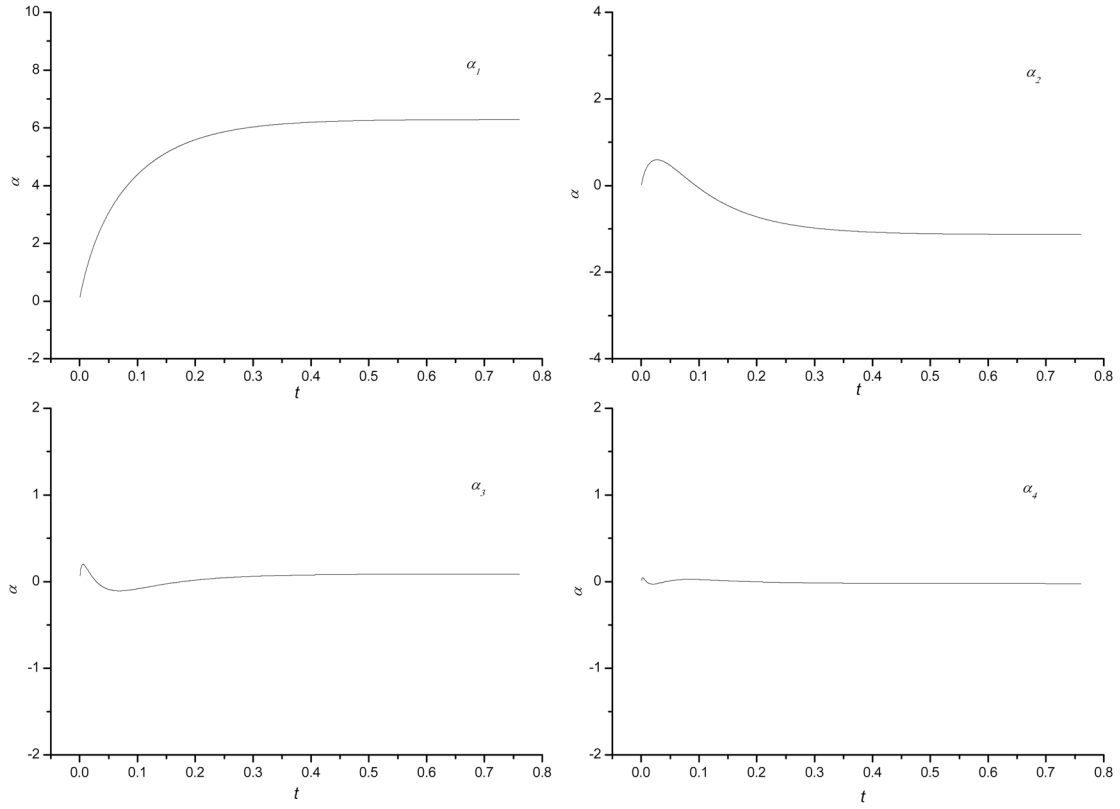

(c)

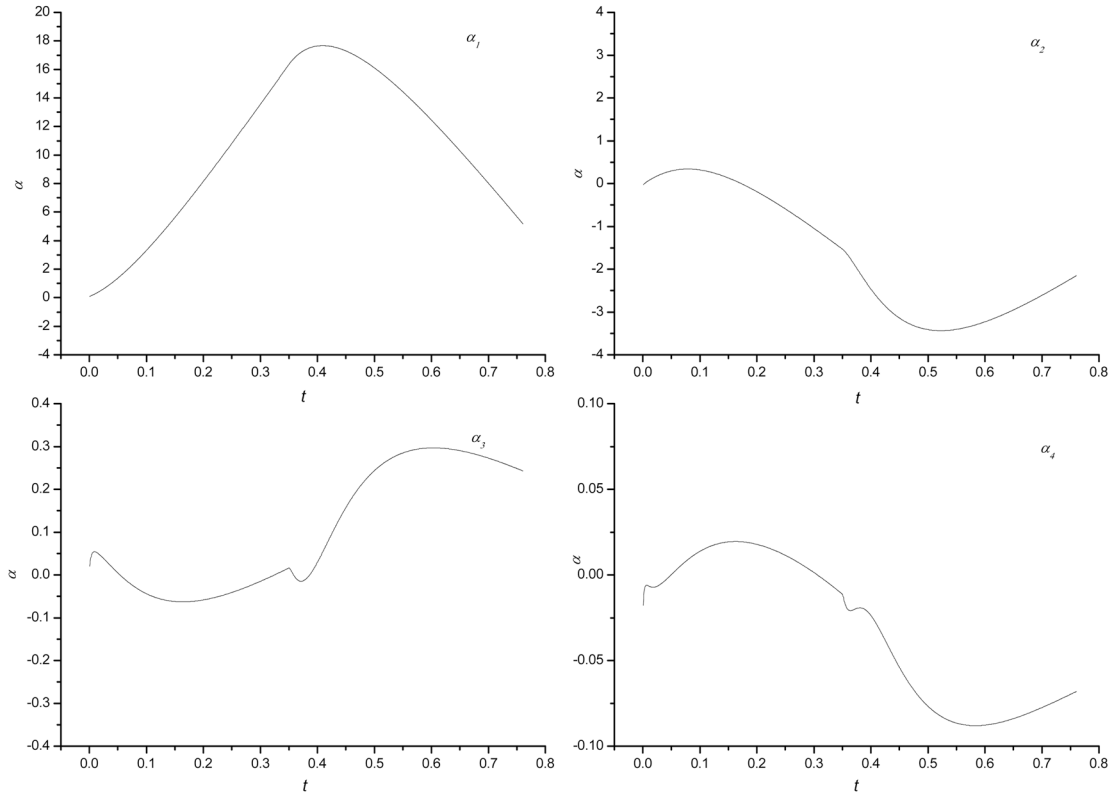

(d)

Fig. 13 (***Continued***).

Downloaded 26 Sep 2008 to 117.32.153.162. Redistribution subject to ASME license or copyright; see http://www.asme.org/terms/Terms_Use.cfm

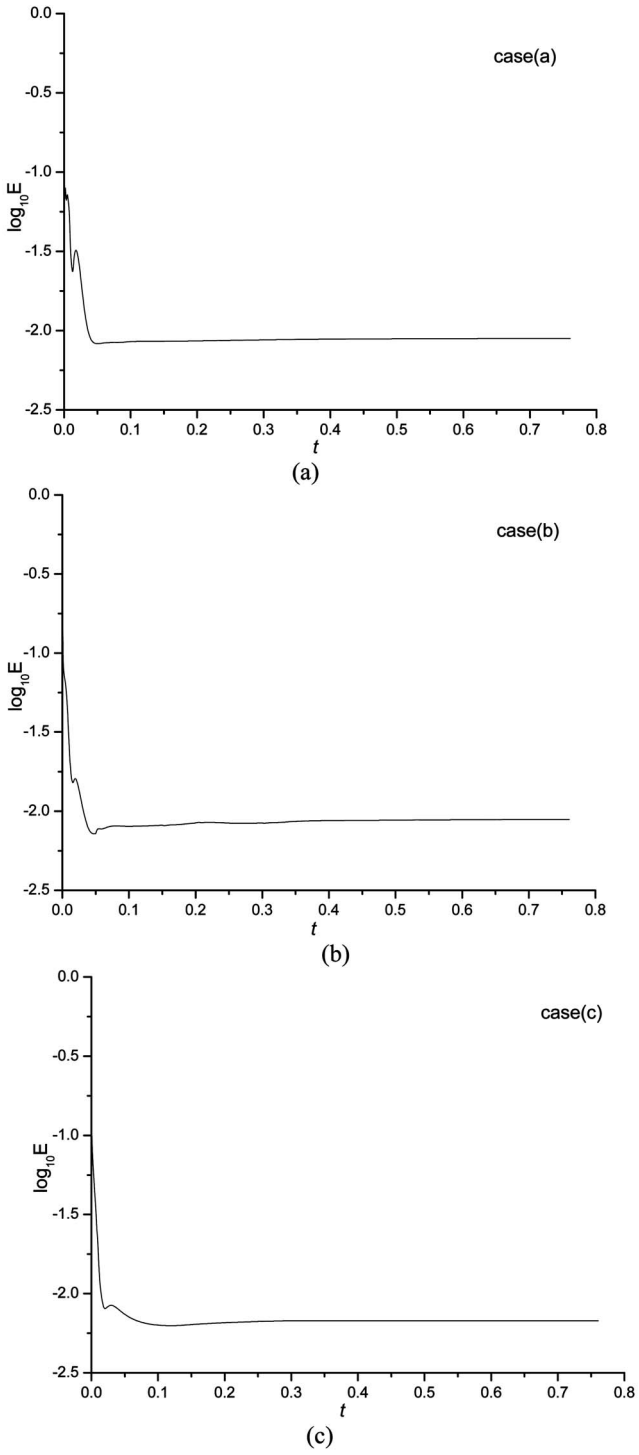

Fig. 14 The temporal variation of relative error between the numerical solutions and the POD solutions for different time-dependent function $f(t)$. (*a*), (*b*), and (*c*) correspond to case (a), case (b), and case (c), respectively.

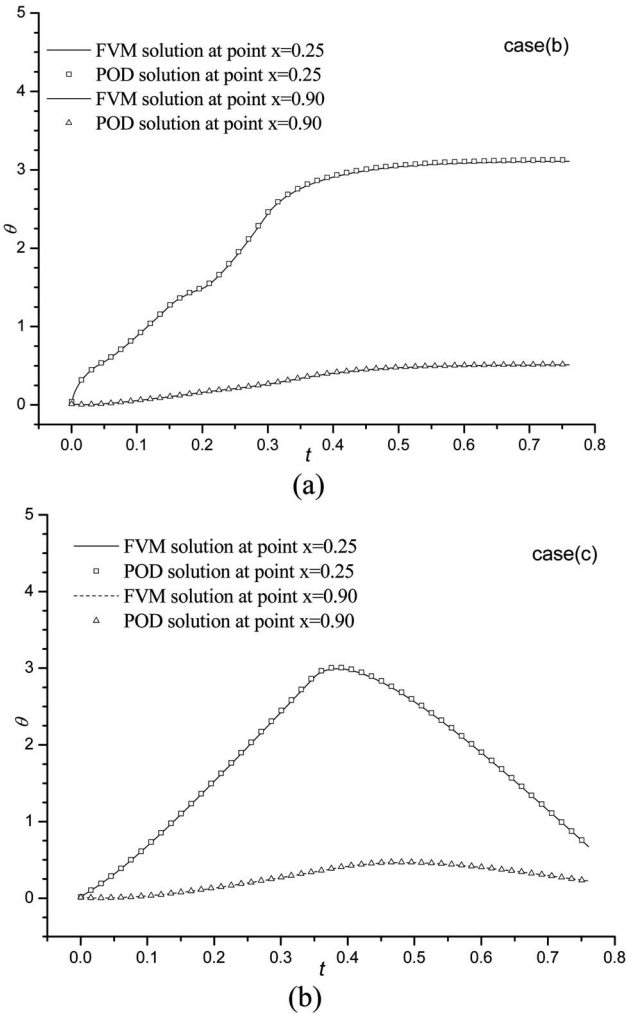

Fig. 15 The temporal variation of temperature at two points for different time-dependent functions $f(t)$. (*a*) corresponds to the case (b); (*b*) corresponds to case (c).

Subscripts

h = hot side
c = cold side
n = the nth or the nth of a vector
POD = physical fields obtained by POD reconstruction

Superscripts

k = the kth column vector

References

[1] Bleris, L. G., and Kothare, M. V., 2005, "Reduced Order Distributed Boundary Control of Thermal Transients in Microsystems," IEEE Trans. Control Syst. Technol., **13**, pp. 853–867.

[2] Azeez, M. F. A., and Vakakis, A. F., 2001, "Proper Orthogonal Decomposition of a Class of Vibroimpact Oscillations," J. Sound Vib., **240**, pp. 859–889.

[3] Kirby, M., and Sirovich, L., 1990, "Application of the Karhunen-Loeve Procedure for the Characterization of Human Faces," IEEE Trans. Pattern Anal. Mach. Intell., **12**, pp. 103–108.

[4] Allery, C., Beghein, C., and Hamdouni, A., 2005, "Applying Proper Orthogonal Decomposition to the Computation of Particle Dispersion in a Two-Dimensional Ventilated Cavity," Commun. Nonlinear Sci. Numer. Simul., **10**, pp. 907–920.

[5] Arjocu, S. C., and Liburdy, J. A., 2000, "Identification of Dominant Heat Transfer Modes Associated With the Impingement of an Elliptical Jet Array," ASME J. Heat Transfer, **122**, pp. 240–247.

[6] Tyagi, M., and Acharya, S., 2005, "Large Eddy Simulations of Flow and Heat Transfer in Rotating Ribbed Duct Flows," ASME J. Heat Transfer, **127**, pp. 486–498.

[7] Berkooz, G., Holmes, P., and Lumley, J. L., 1993, "The Proper Orthogonal Decomposition in the Analysis of Turbulent Flows," Annu. Rev. Fluid Mech., **25**, pp. 539–575.

[8] Holmes, P., Lumley, J. L., and Berkooz, G., 1996, *Turbulence, Coherent Structures, Dynamical Systems and Symmetry*, Cambridge University Press, UK.

[9] Sirovich, L., 1987, "Turbulence and the Dynamics of Coherent Structure. Part I,II,III," Q. Appl. Math., **45**, pp. 561–571.

[10] Patankar, S. V., 1980, *Numerical Heat Transfer and Fluid Flow*, McGraw-Hill, New York.

Downloaded 26 Sep 2008 to 117.32.153.162. Redistribution subject to ASME license or copyright; see http://www.asme.org/terms/Terms_Use.cfm

[11] Tao, W. Q., 2001, *Numerical Heat Transfer*, 2nd ed., Xi'an Jiaotong University Press, Xi'an.
[12] Patankar, S. V., and Spalding, D. B., 1972, "A Calculation Procedure for Heat, Mass and Momentum Transfer in Three-Dimensional Parabolic Flow," Int. J. Heat Mass Transfer, **15**, pp. 1787–1806.
[13] Leonard, B. P., 1979, "A Stable and Accurate Convective Modeling Procedure Based on Quadratic Upstream Interpolation," Comput. Methods Appl. Mech. Eng., **19**, pp. 59–98.
[14] Hortmann, M., Peric, M., and Scheuerer, G., 1990, "Finite Volume Multigrid Prediction of Laminar Natural Convection: Bench-Mark Solutions," Int. J. Numer. Methods Fluids, **11**, pp. 189–207.
[15] Ghia, U., Ghia, K. N., and Shin, C. T., 1982, "High-Re Solutions for Incompressible Flow Using the Navier-Stokes Equations and a Multigrid Method," J. Comput. Phys., **48**, pp. 387–411.

Downloaded 26 Sep 2008 to 117.32.153.162. Redistribution subject to ASME license or copyright; see http://www.asme.org/terms/Terms_Use.cfm